Earth Planets Space, **51**, 863–875, 1999

Response of the airglow OH emission, temperature and mesopause wind to the atmospheric wave propagation over Shigaraki, Japan

H. Takahashi[1], P. P. Batista[1], R. A. Buriti[1], D. Gobbi[1], T. Nakamura[2], T. Tsuda[2], and S. Fukao[2]

[1]*Instituto Nacional de Pesquisas Espaciais, CP-515, 12201-970 São José dos Campos, SP, Brazil*
[2]*Radio Atmospheric Science Center, Kyoto University, Uji, Kyoto 611, Japan*

(Received August 19, 1998; Revised December 30, 1998; Accepted January 17, 1999)

Simultaneous observations of the night airglow OH (6, 2) band emission intensity and rotational temperature, by a sky scanning airglow spectrophotometer, and meteor winds, by a middle and upper atmosphere radar (MU radar), were carried out at Shigaraki (34.9°N, 136.1°E), Japan, from October 29 to November 11, 1994, as the first phase of a campaign, and from July 25 to July 31, 1995 as the second phase. Horizontal structures in the OH emission intensity and rotational temperature were monitored optically, together with the background wind and its wave induced fluctuations, measured by MU radar. Since the MU radar makes a direct measurement of the vertical wavelength, and the OH spectrophotometer makes a direct measurement of the horizontal wavelength, the two techniques are mutually complementary to determine intrinsic wave parameters. Gravity waves with intrinsic periods of 2 to 9 hours, horizontal wavelengths of 500 to 3000 km and vertical wavelengths of 12 to 75 km were identified. Between the two different observation techniques, there is a reasonable agreement in the inferred wave characteristics.

1. Introduction

Recent investigation concerning gravity wave propagation in the middle and upper atmosphere reveals that it plays an important role in energy and momentum transport and further global energy balance in the upper atmosphere (Manson and Meek, 1988; Kato, 1996). Theoretical study of internal gravity waves was started in the 1960's, by Hines (1960), from the phenomenon of wavelike oscillations of ionospheric disturbances. The study of atmospheric waves using temporal variation of the airglow emission was started early in the 1970's. (Krassovsky and Shagaev, 1974; Shefov and Toroshelidze, 1974). Krassovsky *et al.* (1977) investigated the amplitude of oscillation of the emission intensity and the molecular rotational temperature. Imaging observations were first carried out by Moreels and Herse (1977) using a photographic camera and NIR color filter. Peterson (1979) observed wavelike visible and NIR airglow enhancements.

Study of the atmospheric dynamical process (winds and waves) greatly advanced in the 1980's, when MST and MU radar started to measure turbulence, wave propagation and wind in the middle atmosphere (from about 20 km to 100 km) (Manson, 1990; Tsuda *et al.*, 1990). The laser radar (LIDAR) technique has been improved significantly and measured vertical wave propagation in the Na layer (Gardner and Voelz, 1987). In the beginning of 1990's, improvement of imaging cameras using a charge coupled device (CCD) made airglow observations easy to make in the form of an all sky image with relatively short time integration (Taylor *et al.*, 1995a, b). Recent theoretical simulation of airglow response to gravity wave propagation helped to motivate airglow observations (Walterscheid *et al.*, 1994; Makhlouf *et al.*, 1995; Walterscheid and Schubert, 1995).

Characteristics of internal gravity waves vary widely. The wave period varies from a few minutes (Brunt Väisälä frequency limitation) to tens of hours. The horizontal wavelength extends from a few to a few thousands of kilometers. Vertical wavelength also covers from a few kilometers to almost 100 km. However, there is no observation technique to cover all ranges. Each instrument has its limitation in time and spatial resolution. Radar is efficient in covering a large height range, from troposphere to thermosphere, but cannot cover a horizontally extended area. Lidar can also measure vertical wavelengths, with high resolution, but it is difficult to measure spatial variation. Meteor radar can detect meteor echoes continuously, but has its limitation in space (a few hundred km in diameter) and time resolution ($\sim$0.5 hour). In the case of the airglow imager, from short periods (a few minutes) to band-like waves (a few tens of minutes) are well detected (Taylor *et al.*, 1997), but not long waves ($>$1000 km). In order to compensate these limitations and to observe atmospheric waves on a large scale, systematic observational campaigns with the participation of many different instruments have been organized, for example ALOHA/ANLC-1993 (Swenson and Gardner, 1998). In order to study atmospheric gravity waves, source, propagation, and dissipation processes systematically, it is essential to join these different optical and radar techniques.

In our present work, an airglow OH spectrophotometer and MU radar were used to observe time and spatial variation of the OH emission rate and rotational temperature, and time and height variations of the mesopause wind sys-

tem. It is intended that, by measuring these variables simultaneously, the wave parameters—intrinsic wave period and phase velocity, vertical and horizontal wavelengths and propagation azimuth—should be determined without making any assumptions. On the basis of such measurements, the effectiveness of linear gravity wave theory, can be discussed comparing the parameters determined by two techniques. In order to achieve the above mentioned purpose, the MU radar site was chosen to observe the OH airglow. The MU radar meteor mode can cover a gravity wave range similar to that covered by the photometer. Observation has been carried out in two seasons, first in November 1994 and second in July 1995. The number of nights available for the present work was rather small (13 nights), but 12 waves were identified and analyzed.

2. Instrumentation

2.1 MU radar

The Middle and Upper atmosphere (MU) radar is a large atmospheric radar, observing neutral wind and turbulence in the mesosphere, stratosphere and troposphere (as an MST radar), and incoherent scatter from the ionosphere (as an IS radar). The system is a monostatic pulsed Doppler radar. It is an active phased array system consisting of 475 crossed Yagi antennas (Fukao *et al.*, 1985a, b). The main characteristics are summarized in Table 1. The fast beam steering capability with an active phased array system has been used to investigate the detailed structure of atmospheric dynamics, most characteristically for studying gravity waves of small time and height scales in the middle atmosphere (e.g., Tsuda *et al.*, 1989). The flexible system design using computer controlled transmitters and receivers, makes it possible to implement various observational setups for special experiments. Meteor echo observation is one of the special setups available in the MU radar (Nakamura *et al.*, 1991), and this has been applied to observing wind velocities and temperature fluctuations (Tsutsumi *et al.*, 1994). The transmission beam pattern is distorted so as to provide maximum radiation at zenith angles of 30–40° with an isotropic beam pattern in the azimuth direction, in order to increase the meteor echo number (Nakamura *et al.*, 1991). Reception is handled by an array of 4 independent Yagi antennas forming an interferometer, so as to measure the echo arrival direction accurately. In this way meteor echoes are observed in the 75–100 km altitude range over a 200 km diameter horizontal area at 90 km. Details of the transmitting and receiving antennas and data processing procedure have been presented by Nakamura *et al.* (1991).

Table 1. MU radar (meteor radar mode).

Item	Characteristics
Observatory	Shigaraki (34.85°N, 136.1°E)
Antenna system	Circular array of 475 crossed Yagi
Operational frequency	46.5 MHz
Bandwidth	1.65 MHz
Beam width	3.6 deg.
Transmitter	Peak 1 MW, average 50 kW
Aperture	8330 m^2, 103 m in diameter
Beam angle	20 degree from zenith
Time resolution	0.5 hour
Height resolution	1 km

In the meteor radar mode of the MU radar, horizontal wind velocities, N-S and E-W components, are measured, as a function of height from 75 to 100 km, with a height resolution of 1 km. The time integration used to determine the wind vector for the present work was about 30 minutes. Since the operation is continuous, 24 hours a day, this system is advantageous for monitoring tidal oscillations in addition to gravity waves. From the wind profiles, it is possible to derive the vertical phase propagation pattern; consequently, vertical wavelength and period can be derived. The hodograph analysis of wind velocities makes it possible to derive gravity wave parameters using linear gravity wave theory. On the other hand, the OH emission intensity and temperature variation patterns can provide wave period and horizontal wavelength. Two different observation schemes, therefore, complement each other in the investigation of the characteristics of atmospheric waves propagating in the upper mesosphere and lower thermosphere. This is the first simultaneous observation campaign using an OH airglow photometer together with a MU radar. One of the purposes of this campaign was to validate the simultaneous measurements of specific wave parameters using two different techniques and to investigate the limitations of the observational techniques.

2.2 The sky scanning OH spectrophotometer

An advantage of using the OH emission in studying atmospheric waves is that the vibrationally and rotationally excited OH provides two aeronomical parameters. One is the emission rate, which is mainly dependent on the reaction between atomic hydrogen and ozone (Bates and Nicolet, 1950; Takahashi *et al.*, 1992). The other is the molecular rotational temperature. The rotational energy level separation in the $v = 6$ level of OH is of the order of 0.01 eV (see for example, Coxon and Foster, 1982). On the other hand, the kinetic energy level, kT, for the temperature in the mesopause region (200 K) is of the order of 0.02 eV, which exceeds the rotational energy. Therefore the OH rotational population distribution quickly achieves thermal equilibrium after being newly formed. For the lower rotational levels, with rotational quantum number less than 3, this has been confirmed (Pendleton *et al.*, 1993).

Another advantage of the OH emission is that it is relatively easy to measure the OH rotational line spectrum using a rather simple low resolution (around 1 nm) spectrometer. For the present purpose, we constructed a sky scanning spectrophotometer using the tilting filter technique. The main characteristics are listed in Table 2. The OH (6, 2) band $P_1(2)$, $P_1(3)$ and $P_1(4)$ lines were measured by scanning the wavelength from 848 nm to 838 nm. These rotational line intensities are related to the rotational temperature $T(\mathrm{rot})$ in the following way:

$$I_{J'J''} = A(v = 6, J' - v = 2, J'')2(2J'' + 1)/Q(v) \cdot \exp(-F(J', J'')/\mathrm{kT(rot)}) \quad (1)$$

where $I_{J'J''}$ is a rotational line intensity originating from the vibration rotation transition of the excited OH, from J' to J'', A is the Einstein transition probability, $F(J', J'')$ is the rotational energy term, k is Boltzmann's constant and T(rot) is the rotational temperature. The molecular constants for calculation of the OH (6, 2) spectrum were taken from Coxon and Foster (1982). The A values were adopted from the Mies (1974) calculation. New theoretical calculations have been presented by Turnbull and Lowe (1989). There is a systematic difference in the calculated temperature between the two A values. The uncertainty in the absolute value of the temperature due to the choice of the transition probability is around 5 degrees in the present case. Since the purpose of the present work is to study the amplitude of the temperature oscillation, and thus any uncertainty in the absolute temperature is not a concern, the Mies' A values were used in this study as in our previous work.

The intensity ratio between $P_1(4)$ and $P_1(2)$ was used to calculate the rotational temperature. This has a larger temperature dependence compared to other combinations such as $P_1(3)$ to $P_1(2)$. The $P_1(3)$ line was not used because near to the $P_1(3)$ line at 843.0 nm, there are $P_1(12)$ and $P_2(12)$ lines of the OH (5, 1) band, and it is difficult to estimate the contamination due to these lines. The absolute sensitivities of the photometer for the spectral range between 839.9 nm (at $P_1(2)$ line) and 846.5 nm (at $P_1(4)$ line) were calibrated using a MgO screen illuminated by a laboratory sub-standard light source (Eppley ES 8315 calibration lamp). Typical sensitivity is shown in Table 2 as a reference. A portable tungsten light source was used in the field observation in order to check the day to day variation of the sensitivity. Estimated instrumental errors originating from filter transmission functions and uncertainty in absolute sensitivity for the intensity and temperature are $\pm 10\%$ and ± 2 K, respectively. Considering the above mentioned error factors, we estimate that the overall systematic error ranges in the intensity and temperature are $\pm 10\%$ and ± 5 K, respectively, and the random error ranges are $\pm 2\%$ and ± 3.5 K for each measurement.

The photometer has a rectangular diaphragm, 2×10 mm, in order to get a constant wavelength resolution over the 10 nm scanning range. The projection of this aperture in the sky is approximately 2×9.7 km when the photometer zenith angle is 65°. The photometer viewing geometry is shown schematically in Fig. 1. The photometer measured 8 cardinal points in the sky, located on a circle with a diameter of 370 km, making it possible to measure horizontal structure in the OH emission intensity and temperature. This field of view is almost twice as large as that of the MU radar. The photometer time resolution was limited by the wavelength scanning speed, which is 40 seconds to scan the 10 nm range. As a result it takes 6 minutes to complete one sky scanning sequence. With the present observation scheme, therefore, it is not possible to observe waves with periods shorter than 12 minutes and horizontal wavelengths shorter than 280 km (twice the distance between two adjacent points of observation in the sky). Due to the vertical extent of the OH emission layer, about 10 km wide, it is also difficult to identify waves with less than 10 km of vertical wavelength. Most of the image data presented by Taylor *et al.* (1991) , for example, shows the presence of short waves with lengths of a few tens of kilometers. With our present method, however, it is not possible to identify such short waves. The finite field of view (around 40 degrees full angle) of the MU Radar, as mentioned later, also limits the response to small scale structures.

Table 2. OH spectrophotometer characteristics.

Item	Characteristics
Aperture	6.2 cm
Field of view	2.9×0.6 deg. (rectangular)
Wavelength resolution	1.15 nm
Wavelength scanning range	848–838 nm (tilting filter)
Detector	PMT (Ham. R943-2)
Overall sensitivity at 840 nm	14 cps/Rayleigh
Sky scanning	Single rotating mirror
Observation zenith angle	65 deg.
One sky scanning sequence	6 min.

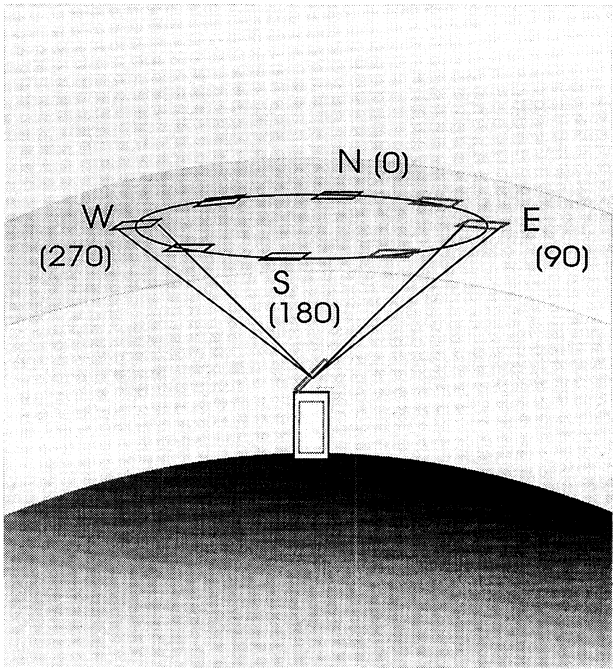

Fig. 1. Schematic view of the photometer observation directions.

2.3 Limitations in identification of atmospheric waves from the two methods

As mentioned above, the OH photometer observes wave period, horizontal wavelength and phase velocity, and propagation direction. The MU meteor radar, on the other hand, observes wave period, vertical wavelength and phase velocity in addition to wind velocity. The photometer and the MU radar meteor wind measurements each have their intrinsic time and spatial limitations. In Table 3, the observational limitations of the two techniques are summarized. This is based on the principle that the minimum observable wave-

Table 3. Observational limitations of the OH photometer and the MU radar wind measurements.

	Period, T (h)	λ_x (km)	λ_z (km)
Photometer	0.2–9	280–∼3200	(10–∞)
MU radar wind	1.0–∞	(400–∞)	2–40

Note: The values in parentheses are not directly observable.

length and period should be equal to twice the instrumental resolution. As mentioned in the previous section, the photometer time and spatial resolutions are about 0.1 hr and 140 km, respectively. The longest period measurable can not exceed the duration of the data sequence, normally 9–10 hrs. Maximum horizontal wavelength is dependent on uncertainty in the calculation of the phase difference. In the present case this was 20°, which corresponds to approximately 3200 km. The vertical wavelength is dependent on the OH emission layer thickness, which is around 8–10 km. On the other hand, the MU radar works with 1/2 hour time integration and a 200-km diameter area of the sky at around 90 km height. The vertical resolution is 1 km. Since the height range for measurements with a reasonable level of precision is limited to about 78 to 98 km, the maximum vertical wavelength that can be determined with reasonable accuracy will be about 40 km.

An advantage of the simultaneous measurements using the two techniques also lies in the calculation of the intrinsic wave parameters, period and phase velocity, using the background wind data provided by the MU radar. In the mesopause region the background wind velocity is normally small but vertical wind shear occurs frequently, disturbing the airglow emission layers in this region. Information on the wind profile, therefore, is of essential importance for investigating the response of the OH intensity and rotational temperature to the passage of gravity waves.

3. Observations

3.1 General features

The airglow OH (6, 2) band intensity and rotational temperature measurements, at the Shigaraki (34.9°N, 136.1°E) MU radar site, were carried out in the first stage from October 29 to November 11, 1994, and in the second stage from July 24 to 31, 1995. After the campaign in July, the airglow observation was continued up to September 18. During the course of the campaign, the MU radar was operated continuously in the meteor radar mode for one week. In Table 4, the OH and meteor radar data obtained during the two periods are listed. For the present study only the period when both OH and meteor radar data are available are used. In the November 1994 data, from a total of 7 nights of useful simultaneous OH and wind measurements, 5 nights showed wavelike variations not only in the band intensity but also in the temperature. In the July 1995 data, surprisingly, all of the nights showed clear wave propagation features. A given night is considered to show the presence of wavelike oscillations when a periodic oscillation could be found in both the emission intensity and temperature variations and at least three directions show the same period of oscillation.

Table 4. Chronological list of the airglow OH and meteor wind measurements carried out at Shigaraki, Japan. The radar operated continuously from Nov. 3–11 and from July 24–30.

	Date	OH Obs. (hs.)	MU Obs.
1	1994 Oct. 29	4	
2	Oct. 30	8	
3	Oct. 31	10	
4	Nov. 03	6	*
5	Nov. 04	9	*
6	Nov. 07	3	*
7	Nov. 08	8	*
8	Nov. 09	5	*
9	Nov. 10	5	*
10	Nov. 11	5	*
11	1995 July 24	8	*
12	July 25	6	*
13	July 26	7	*
14	July 27	7	*
15	July 28	8	*
16	July 29	7	*
17	July 30	8	*
18	July 31	8	

The zonal and meridional wind components as a function of height and time during the observation period of July 1995 are shown in Fig. 2. As can be noted from the figure, the wind pattern demonstrates periodic changes in direction and amplitude, consistent with tidal oscillations, but with significant day to day variations. It is also interesting to note that the zonal wind is stronger than meridional wind.

3.2 Tides

The periodic oscillation pattern in Fig. 2 demonstrates the importance of tidal oscillation. In Fig. 3, daily oscillation patterns of the wind components (u and v), averaged over the July 95 period and November 94 period are shown. The July 95 wind shows a strong tidal oscillation pattern with diurnal and semi-diurnal components. On the other hand, the amplitude of oscillation of the November 94 wind is small. Tsuda *et al.* (1988) reported that semi-diurnal tidal oscillation of the eastward wind were larger in July than November/December. Our present results agree with them. Averaged vertical wind profiles for the July 95 data, shown in the figure (bottom left side), show a vertical wavelength of about 28 km. Such short wavelengths suggest the importance of the diurnal component. On the other hand, the November 94 data did not show significant vertical wave structure, suggesting that the vertical wavelength was much longer than 40 km.

Average nocturnal variations of the OH intensity and rotational temperature shown in Fig. 4 demonstrate different time variations in July 95 and November 94. The July data has a

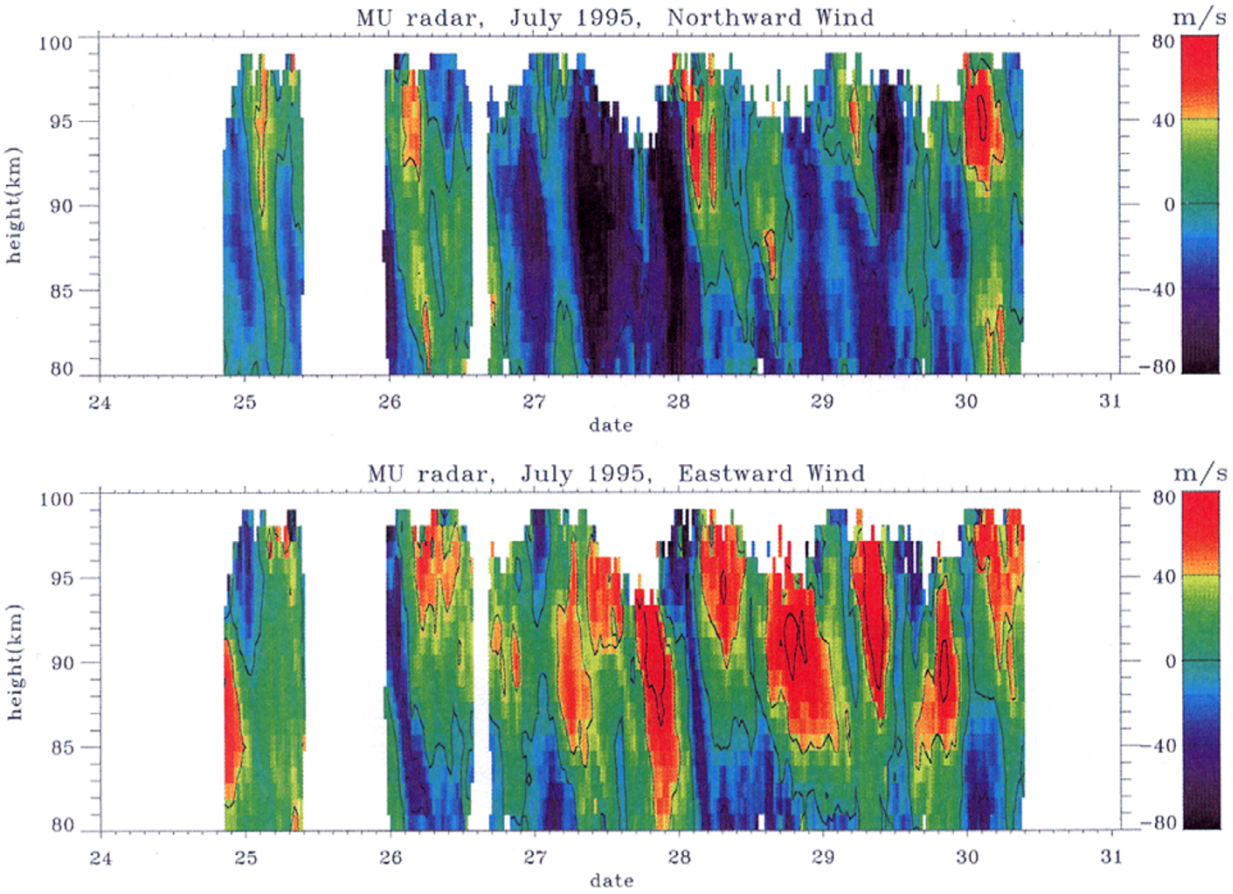

Fig. 2. Observed wind structure as a function of height and time from July 24 to July 30. Northward and Eastward are positive.

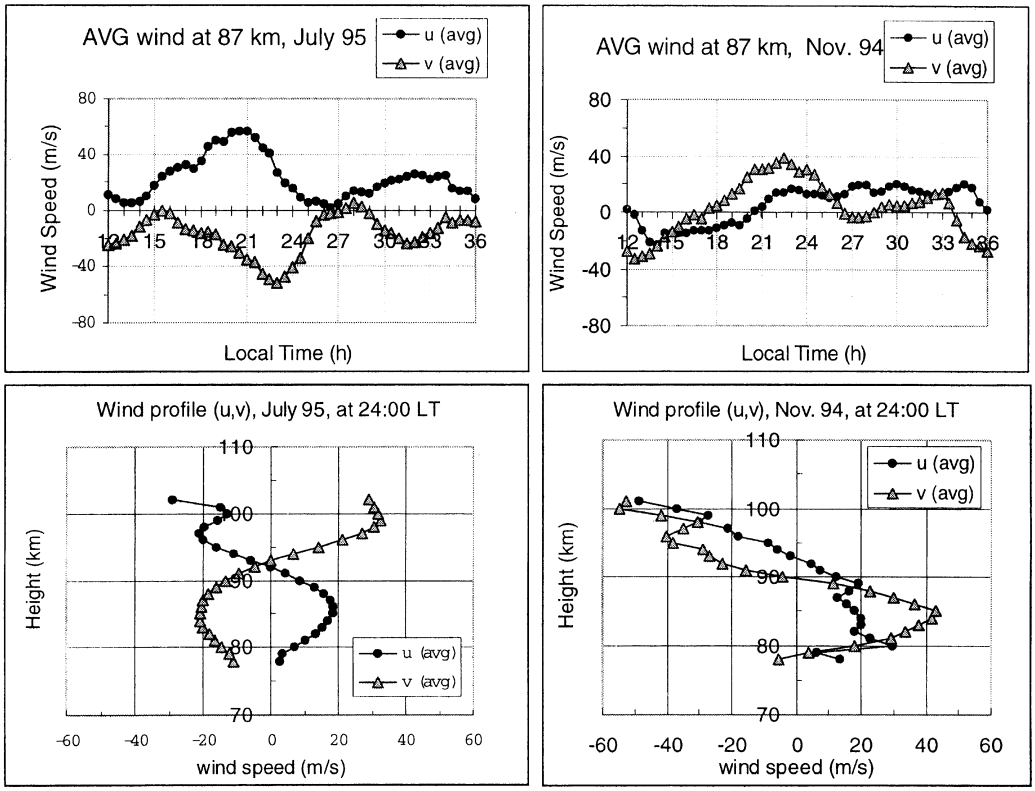

Fig. 3. Average wind, u and v, variations at 87 km height (top), and average wind profiles, u and v, at 24:00 LT (bottom).

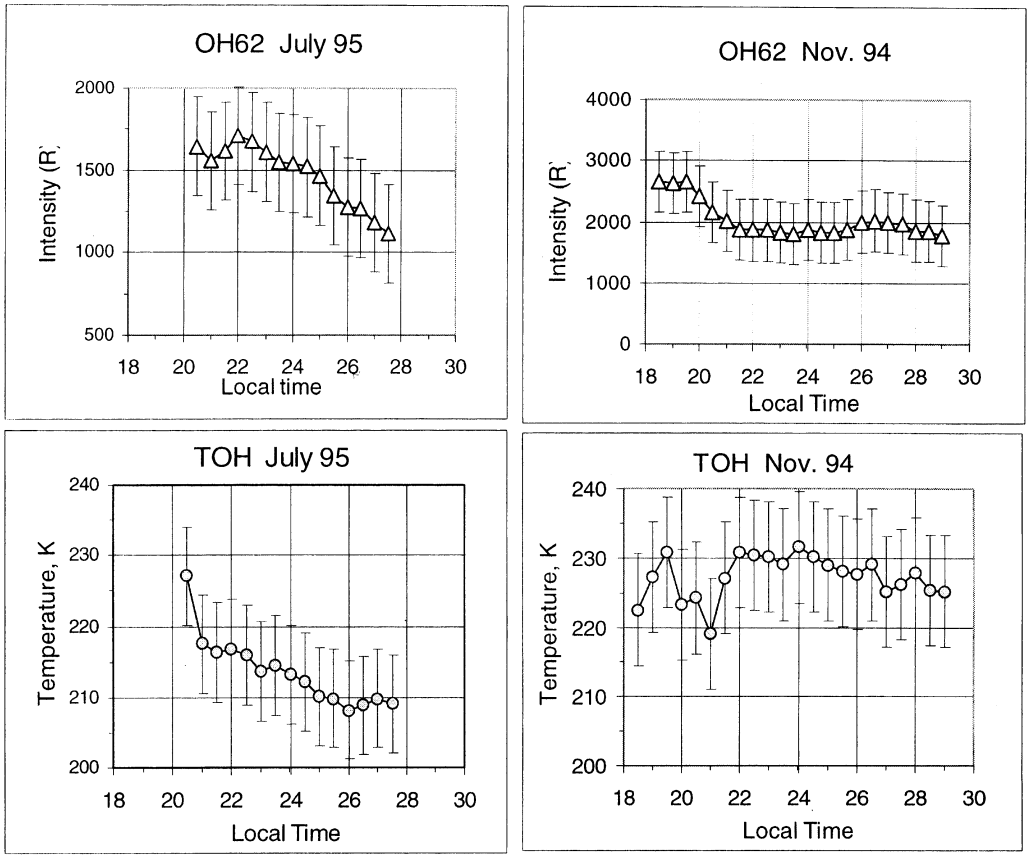

Fig. 4. Monthly averaged nocturnal variations of the OH (6, 2) band intensity and rotational temperature for November 1994 (right side) and July 1995 (left side).

tendency for monotonic decrease during course of the night, while the November 94 data showed an increase after midnight, suggesting a short period (~12 h) oscillation. Tidal (diurnal and semidiurnal) oscillations play an important role in the mesopause region, frequently having an amplitude of oscillation comparable to that of gravity waves. In order to study gravity waves, therefore, they should first be subtracted from the data.

3.3 Nocturnal variations

Nocturnal intensity and temperature variations for individual nights show complicated features. In Figs. 5, 6, and 7, some notable oscillation patterns are shown. Nocturnal variation of the OH emission rate for 8 directions are plotted in 3 dimensional form. As a typical nocturnal variation, Fig. 5 (August 29) shows a peak intensity around midnight, decreasing to early morning. No phase lagged oscillations between the different directions were observed. Such variations are normally generated by tides.

The night of July 26, shown in Fig. 6, is rather disturbed. A large amplitude wave first appears in the E direction around 22 h propagating to N, followed by a second wave, appearing in the NW around 24:30 h and propagating to S. This spatial oscillation gave a large intensity gradient in the NE-SW direction. The rotational temperature also showed a similar oscillation. On the night of July 30 (Fig. 7) a double peaked structure can be seen. The first peak at around 21 h did not show any phase lag between the directions. The second peak,

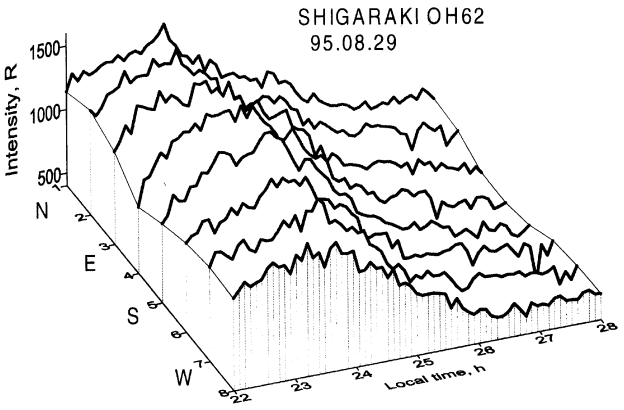

Fig. 5. Three dimensional view of the nocturnal variation of the OH (6, 2) band intensity at the 8 directions, from top (N) to down (NW), for August 29, 1995.

close to 24–25 h, however, showed a phase lag indicating a wave propagating from the S to N direction. This can be interpreted as a gravity wave superposed on a tidal wave.

4. Data Analysis

4.1 Wave characteristics derived from the OH airglow

The purpose of the present study is to obtain the wave parameters, period, τ, phase velocity, v_p, horizontal wave-

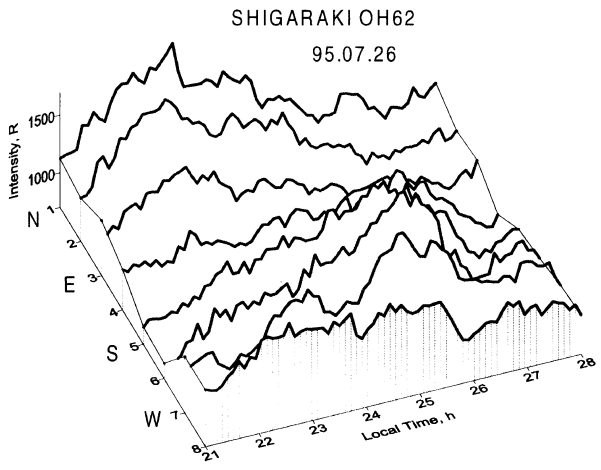

Fig. 6. Same as Fig. 5, except for July 26, 1995.

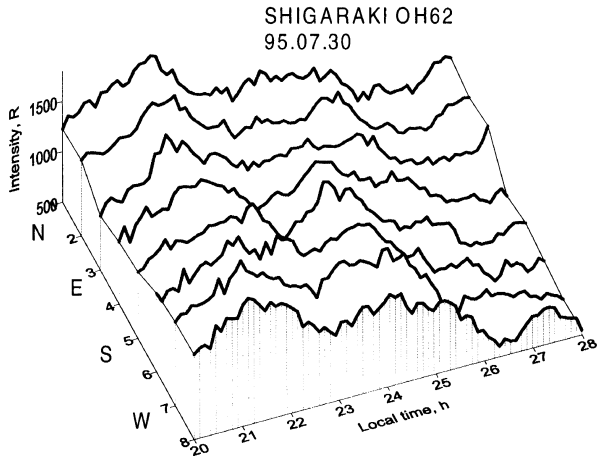

Fig. 7. Same as Fig. 5, except for July 30, 1995.

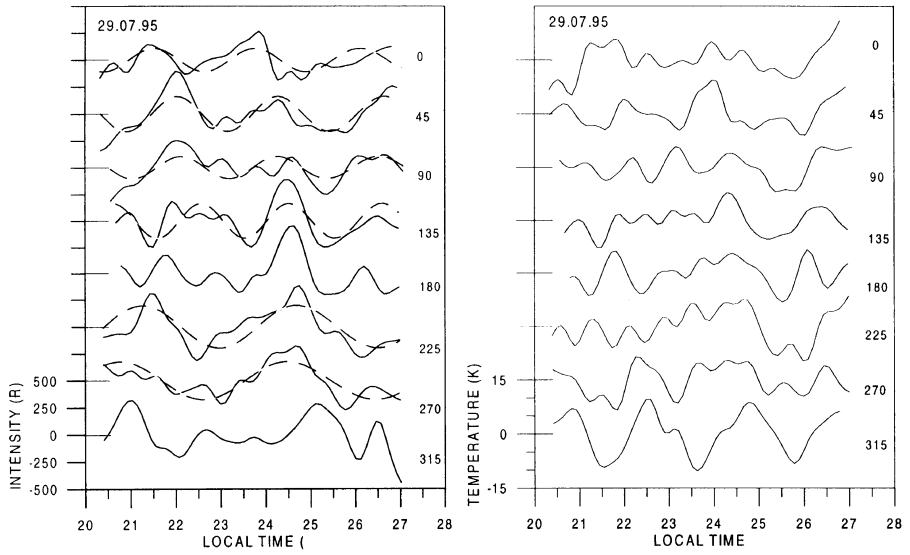

Fig. 8. Nocturnal variations of the OH(6,2) band emission intensity (left) and the rotational temperature (right) on July 29, 1995, at 8 cardinal points of the sky at a zenith angle of 60°. The dashed lines show harmonic functions, frequencies of which were obtained by using MESA analysis (see text).

length, λ_x, and vertical wavelength, λ_z, from observed wave patterns. Our present airglow photometer and the observation mode employed only lets us observe waves with periods longer than 0.2 hours and horizontal wavelength longer than 280 km. Despite the limited range of our observations, on some occasions we observed two waves propagating simultaneously, with different directions and wavelengths. For the purpose of the current analysis an oscillation is assumed to be caused by a propagating wave when (1) the amplitude is more than 3 times the standard deviation of the individual data samples averaged in each plotted value in more than three directions, (2) the temperature also shows a similar oscillation. In this analysis, periods of less than 1.5 hr were omitted because of low significance levels and/or lack of coherence between the intensity and the temperature oscillations. As an example, nocturnal variation patterns of the intensity and temperature of the night of July 29 are shown in Fig. 8. A wave structure can be seen at 21–22 hs and 24–25 hs. The temperature variations also show wavelike oscillation around midnight.

In order to determine wave periods from the nocturnal variations of the emission intensity and rotational temperature, the Maximum Entropy Analysis method (hereafter MESA) was applied to both the intensity and temperature data from the OH photometer, and to the MU radar wind data. In applying the method, Burg's algorithm (Anderson, 1974) was used with a filter order of 40% series length. In order to avoid peak splitting, we used a Hamming window (Kaveh and Lippert, 1983) as a weighting function in calculating the reflection coefficient. After finding the wave periods, their phase and amplitude were obtained from ordinary Multiple Regression Analysis. The data analysis procedure adopted is shown in a flowchart as Fig. 9. The MESA analysis power spectrum of the OH (6, 2) band intensity variations for the night of July

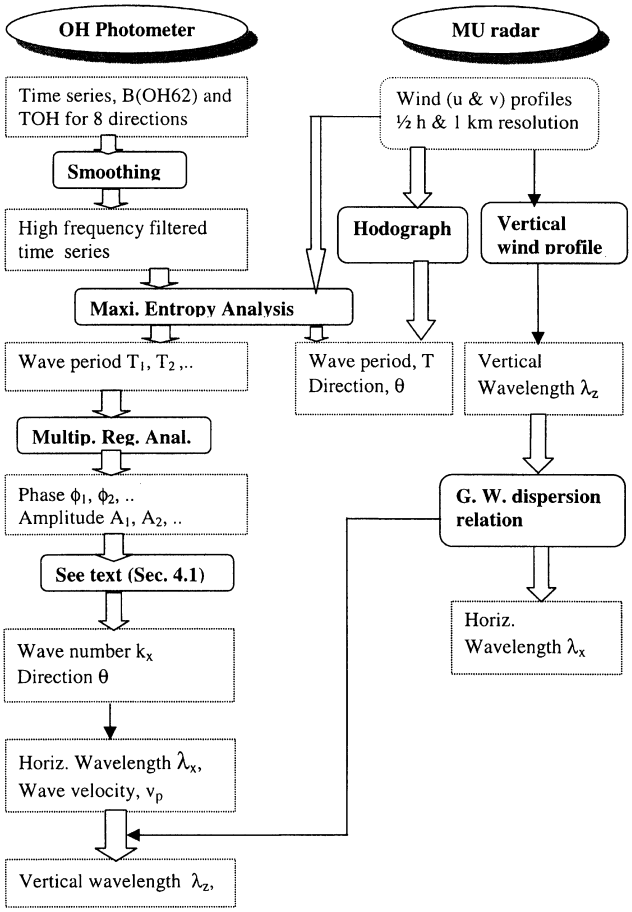

Fig. 9. Flow Chart for calculation of wave parameters from the OH airglow data (left side) and the MU radar meteor wind data (right side).

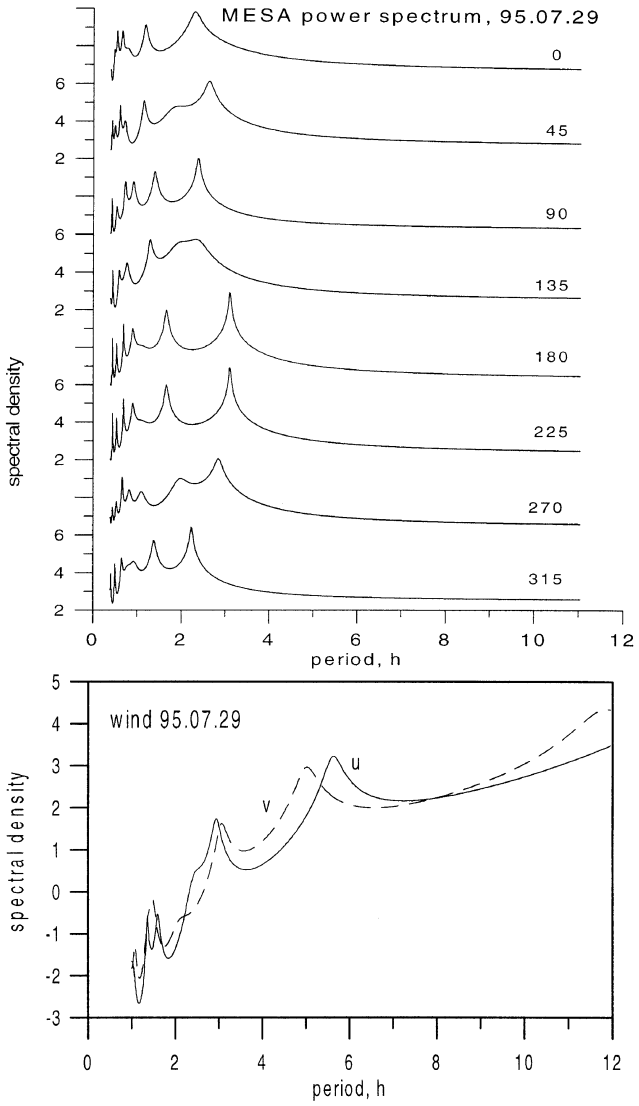

Fig. 10. MESA analysis power spectrum of the OH (6, 2) band intensity variation (top) and wind, u and v, components on July 29, 1995.

29 is presented in Fig. 10. In this analysis longer period (12 and 6 h) oscillations are filtered out. An oscillation period of around 2 to 3 hours can be clearly seen, except in the S and SW directions. Applying the spectral analysis to the time series of the OH intensity of July 29 a wave with a period of 2.2 hr was identified, shown in Table 5 as an observed period, τ_o. Also shown in Fig. 10 is the power spectrum of the wind components. Both u and v components demonstrate periods at around 3 and 5 hours, which are not in agreement with those obtained by the OH data. It should be noted here that these periods are observed ones and include the Doppler effect by the background wind. Intrinsic periods must be deduced and this will be discussed below.

Wave parameters, horizontal wavelength (λ_x), direction of propagation (θ) and phase velocity (v_p) can be derived from the phase differences between the time series for the 8 directions as shown for O_2 Atmospheric band emission oscillations by Zhang *et al.* (1993). Referring to Fig. 11, a plane wave which propagates in the x direction, with an angle of θ measured from North, with wave number k_x can be expressed as,

$$F(t, x) = A\cos(\omega t - k_x x) \tag{2}$$

with its phase being $\Phi = k_x x$.

The phase difference $\Delta\Phi$ between the wave observed at two points in the sky, for example P_I and P_J in the figure, can be expressed as

$$\begin{aligned}\Delta\Phi = \Phi_J - \Phi_I &= k_x r[\cos(J-\theta) - \cos(\theta - I)] \\ &= k_x \sin\theta r(\sin J - \sin I) + k_x \cos\theta r(\cos J - \cos I)\end{aligned}$$

or

$$= ar(\sin J - \sin I) + br(\cos J - \cos I) \tag{3}$$

where

$$a = k_x \sin\theta \quad \text{and} \quad b = k_x \cos\theta.$$

The two unknowns, "a" and "b", can be determined if we have at least two equations, i.e., phase differences between 3 directions. In practice, it was possible to use more than 4 directions for extended wavelike oscillations. Therefore the least square method was applied to find out the unknowns from a linear relationship between $r(\sin J - \sin I)/\Delta\Phi$ and $r(\cos J - \cos I)/\Delta\Phi$. The horizontal wavenumber k_x and wave direction θ, therefore, can be expressed from the rela-

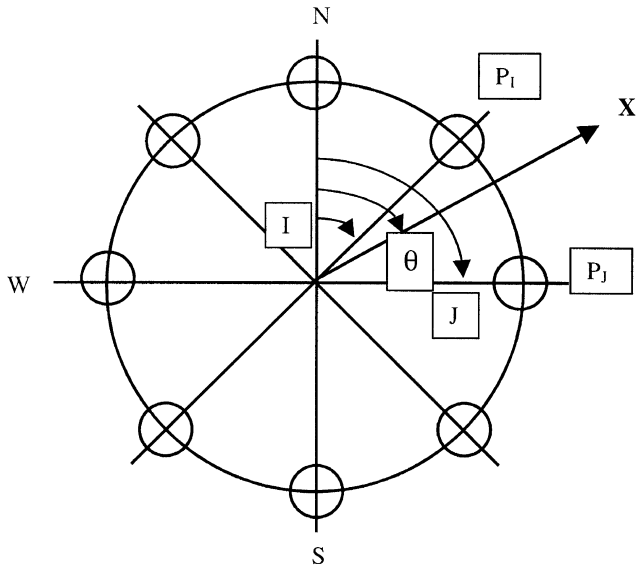

Fig. 11. Geometric relationship of the wave propagation direction, X, with an angle of θ measured from $N(0)$, two observation directions, P_I and P_J in question, and their angle I and J.

tion between "a" and "b",

$$k_X = (a^2 + b^2)^{1/2}, \tag{4}$$

$$\theta = \tan^{-1}(a/b). \tag{5}$$

In this calculation we used a method similar to that developed by Zhang *et al.* (1993). Once the wave number, k_x, is decided, the horizontal wavelength can be obtained in the usual way,

$$\lambda_x = 2\pi/k_x. \tag{6}$$

The phase velocity, v_p, is then calculated from the relation

$$v_p = \lambda_x/T. \tag{7}$$

In order to get the intrinsic phase velocity and period the background (BG) wind components should be estimated and subtracted from the observed phase velocity. It is, however, not easy to estimate the background wind components because the vertical wind profile is strongly modulated during the passage of a gravity wave. In this study, we estimated the winds from vertically averaged meridional and zonal wind components between 85 and 95 km for 6 hours centered on the time of wave occurrence. The estimated BG wind in this way is about 40 m/s on July 29. Once the BG wind is determined the intrinsic period, τ_i, is given by,

$$\tau_i = \lambda x/(v_o - G_x) \tag{8}$$

where G_x is the BG wind velocity in the direction of the wave propagation. The observed oscillation period, horizontal wavelength, phase velocity and the direction of phase propagation calculated in this way are summarized in Table 5. It should be noted that intrinsic phase velocity and the BG wind speed are in same magnitude and is about twice as large as the observed period owing to the Doppler effect. The values shown in parentheses are the standard deviations

Table 5. Wave parameters, observed and inferred from OH airglow and meteor winds for July 29, 1995.

Item	OH	MU
Period (observed), (hr)	2.2 (0.2)	2.9 (0.5)
Period (intrinsic), (hr)	4.5 (0.5)	5.6 (0.3)
λ_x (km)	613 (100)	695 ∗ (50)
λ_z (km)	11.4 ∗ (2)	11 (1)
Phase vel. (m/s) Obs.	78 (10)	—
Phase vel. (m/s), intrinsic	38.5	35
Direction, θ (deg.)	131 (10)	108 (10)
BG wind, v_{BG} (m/s)	39.5 (5)	39.5

Note: The asterisk (∗) indicates values inferred using the gravity wave linear dispersion relationship. The values in parenthesis are statistical error range. θ indicates direction of propagation measured clockwise from $N(0)$.

of the values observed in the different directions, which are much larger than the errors propagated from other sources.

The vertical wavelength can be inferred from gravity wave linear dispersion relation theory,

$$(\lambda_x/\lambda_z)^2 = (N^2 - \omega^2)/(\omega^2 - f^2) \tag{9}$$

where λ_x and λ_z are horizontal and vertical wavelengths, respectively, and N is the Brunt Väisälä frequency. Assuming an isothermal atmosphere, N is estimated to be 3.26×10^{-3} c/s, corresponding to the period of 5.1 minutes, using the averaged temperature, 216 K for the night of July 29. The parameter ω is the intrinsic frequency of the wave and f is the Coriolis parameter

$$f = 2\Omega \sin\varphi \tag{10}$$

which can be determined by the Earth's rotation angular velocity Ω and the latitude φ. At the MU radar site it is 1.33×10^{-5} c/s. The results for λ_z calculated in this manner are also listed in Table 5.

4.2 Wave characteristics derived from meteor wind

In Fig. 12 vertical wind profiles are shown from 20 to 28 hs with a time interval of 1 hour. The BG wind was subtracted in the figure. Short vertical wavelength oscillations, around 10 km, propagating downward can be seen in both u' and v'. In the case of the passage of a gravity wave, it is predicted from the theory that the perturbed horizontal wind components u' and v' should be out of phase when the period is long and the Coriolis factor significant. In order to examine this point, hodographs (Tsuda *et al.*, 1990) of the u' and v' components as a function of height for the night of July 29 are also shown in Fig. 12. The plots (u', v') are time averaged values between 19:00 LT and 20:00 LT. The locus of the plotted points is well represented by an ellipse. It can be seen that the wind components (u', v') rotate clockwise with height increasing from 87 km to 96 km, suggesting that the wave energy is propagating upwards and its phase propagating downwards and that the direction of the wave propagation is parallel to the semi-major axis (Tsuda *et al.*, 1990).

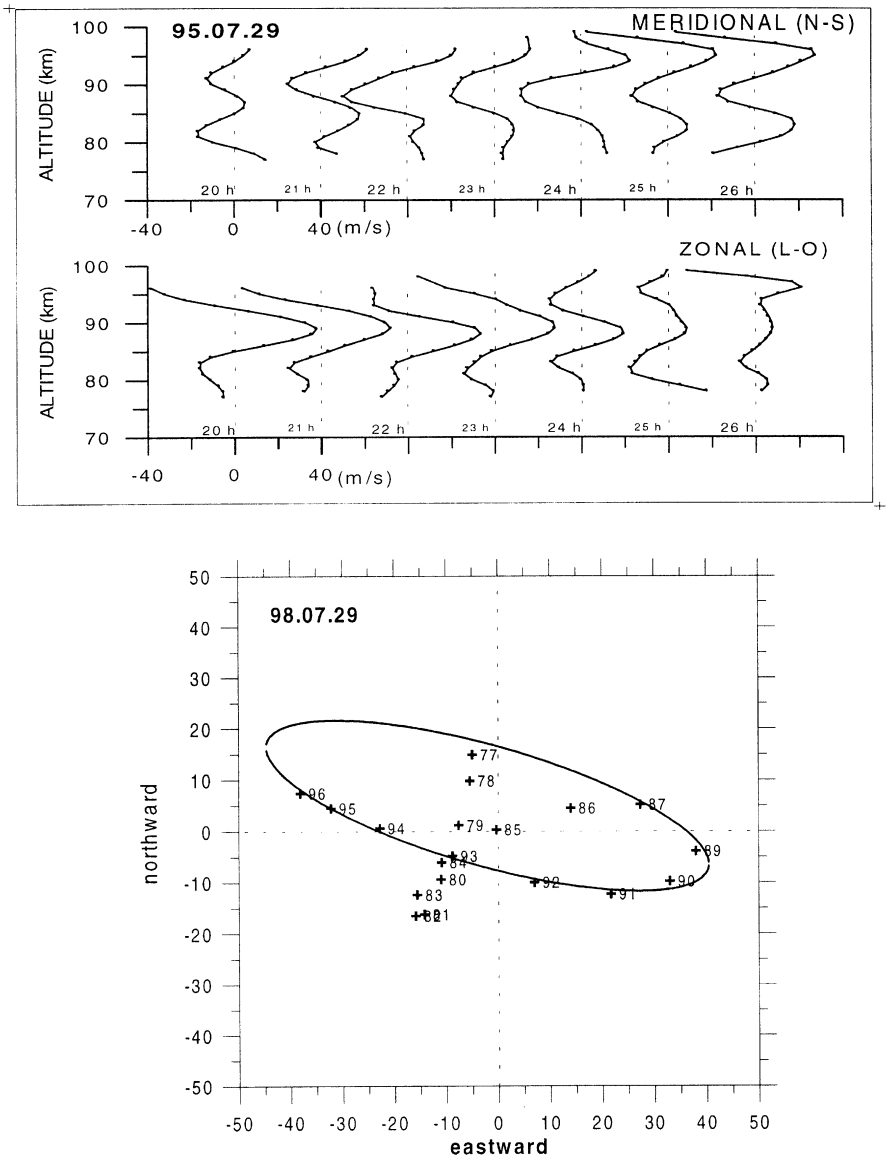

Fig. 12. Hourly averaged vertical wind profiles as a function of height for July 29, 1995 (top) and hodograph of the wind components u' and v' (bottom). The curved line is a least square fit of a ellipse to the hodograph.

According to the polarization relation of gravity wave theory, the intrinsic frequency of the wave can be estimated from the relation

$$V/U = -i(f/\omega) \tag{11}$$

where U and V are horizontal perturbation velocities parallel and perpendicular to the direction of the wave propagation, ω is the intrinsic frequency of the wave and f is the Coriolis parameter. From the Hodograph, the values U from the semi-major axis and V from the semi-minor axis are 44.5 m/s and 12.0 m/s, respectively. The intrinsic frequency of the wave, therefore, can be estimated as 4.93×10^{-5} Hz, corresponding to a period, 5.6 ± 0.2 hours. This is a typical period seen in MU radar mesospheric observations (Nakamura *et al.*, 1993). The horizontal wavelength, λ_x, can be estimated from the linear dispersion relation, Eq. (9). The horizontal wavelength obtained in this manner is 695 km. It is longer than observed by the photometer. From the time series of the wind data it is also possible to determine (observed) wave period using the MESA analysis mentioned above. Vertical wavelength was also determined from the phase difference in the time series between the different altitudes. The results are summarized in Table 5.

Comparing the results of the OH and MU radar in Table 5, there is good agreement in the wave parameters obtained from the airglow and the winds. The difference in the intrinsic period between the OH and MU is somewhat large, almost one hour. It must be due to large errors originating from the estimate of the BG wind, since the latter is of the same order of magnitude as the phase velocity. Fairly good agreement can be seen not only in the horizontal and vertical wavelengths, but also in propagation azimuth. Thus the measurements made by the two different techniques can be interpreted as referring to the same wave. It can be further

Table 6. Summary of wave parameters obtained from the November 1994 and July 1995 data.

Event	Day	Period, h	$\lambda(h)$, km	$\lambda(z)$, km	$V(p)$, m/c	Azimuth (θ)
1	94.10.31	3.5	1172	29	93	306
2	94.11.03	7.3	1056	12	40.2	318
3	94.11.04 (1)	9.2	2960	24.5	86	190
4	94.11.04 (2)	2.9	2540	75.7	243	185
5	94.11.08 (1)	9.7	2409	20	69	347
6	94.11.08 (2)	3.8	512	12	37	341
7	95.07.24	4.6	915	16.6	55.8	130
8	95.07.25	2.1	481	19.6	62.3	36
9	95.07.26 (1)	5.5	1592	23.4	79.8	282
10	95.07.26 (2)	4.4	1552	28.8	97.7	144
11	95.07.27	4	1880	38.9	131.3	52
12	95.07.29	4.5	613	11.4	38.5	131

said that linear gravity wave theory can be effectively used in order to infer the wave parameters.

5. Results and Discussion

Observed gravity wave characteristics

The wave analysis was applied for the November 94 and July 95 data groups, a total of 13 nights. The results are summarized in Table 6. A part of the November 94 data has been reported elsewhere (Takahashi *et al.*, 1998). The intrinsic period varies between 2 and 9.7 hours. Horizontal and vertical wavelengths cover a wide range from 480 to 2900 km and 12 to 76 km, respectively. It is interesting to note that the long period (∼9 h) and long wavelength (more than 2000 km) waves observed in November can not be seen in the July data. Tsuda *et al.* (1990) reported such long waves in the month of October. The waves seen in the July data are rather short period, around 2 to 5 hours.

Differences in the wave characteristics between July and November can be seen in the propagation azimuths. In Fig. 13 the azimuths are shown for the November group (top) and the July group (below). The time evolution of the wind vector (u, v) during the night from 18 to 30 hrs is also presented in order to show the background wind field. Each plot is an average of 6 nights at 87 km height. The wave propagation azimuths for the November data are biased to NW and S. The wind vector shows, however, mainly the NE direction around midnight. On the other hand, the July group does not show any tendency in azimuth. Three waves are oriented in the same direction as the wind. Similar propagation properties were presented by Nakamura *et al.* (1993). They showed dominant SE and SW propagation in October and SW and NW propagation in November. Tsuda *et al.* (1990) have reported dominant southward propagation in October. Our present results, therefore, agree with the previous studies. The change of the wave direction from October to November could be due to a seasonal change of the wind field in the lower atmosphere.

Figure 14 summarizes the present results in a plot of the

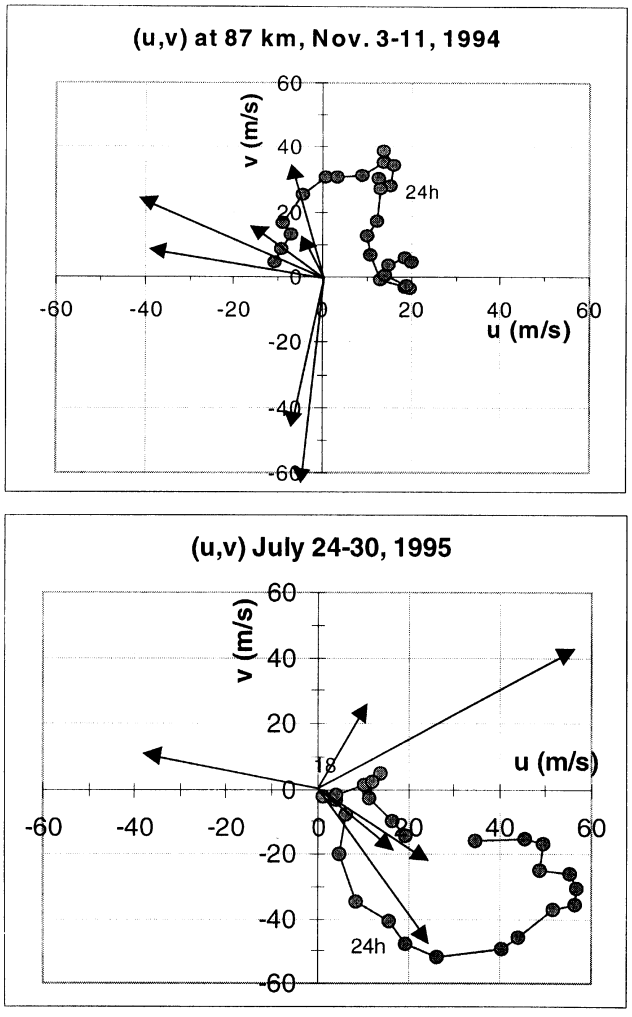

Fig. 13. Wave propagation azimuths (arrows) and averaged wind (u, v) time evolution at 87 km, from 18:00 to 30:00 LT (circles), for November 94 group (top) and July 95 group (bottom).

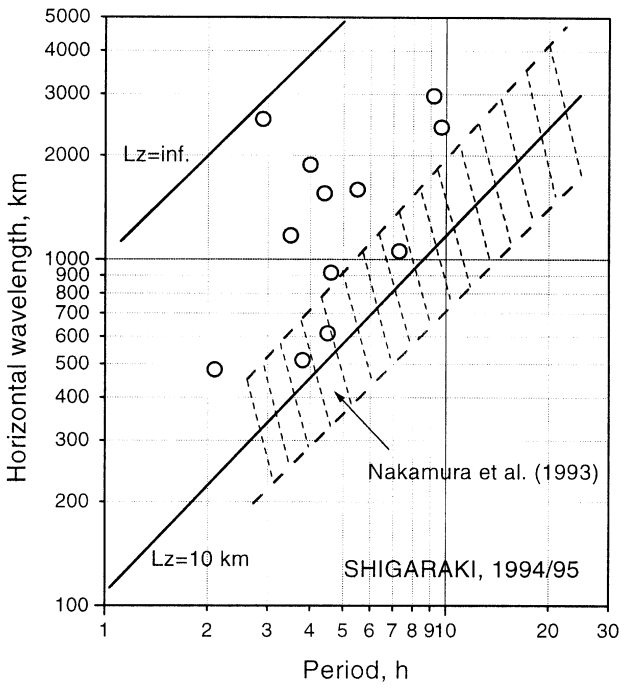

Fig. 14. Scatter diagram of intrinsic period versus horizontal wavelength of the wave events observed on November 1994 and July 1995. Solid lines indicate the extreme limit for vertical wavelength of $\lambda z = 10$ km and $\lambda z = \infty$ (inf.). Dashed area shows the data by Nakamura *et al.* (1993).

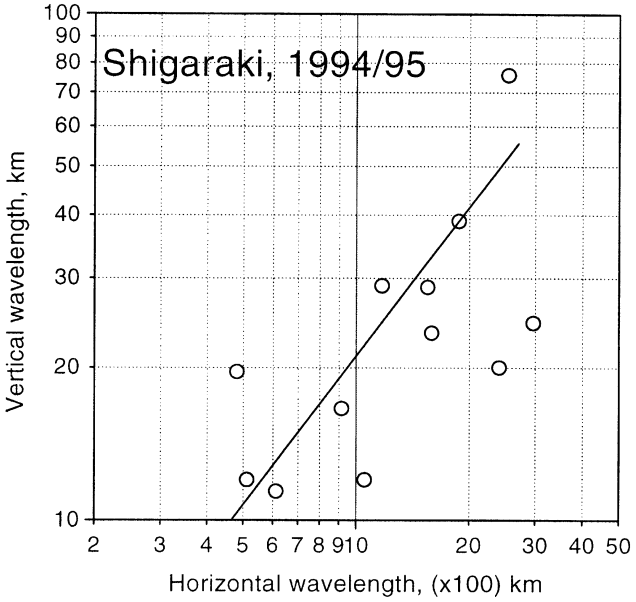

Fig. 15. Horizontal wavelength versus vertical wavelength of the wave events observed on November 1994 and July 1995. Solid curve indicates horizontal and vertical wavelength relation with a fixed wave period of 4.0 hour derived from the linear gravity wave theory.

horizontal wavelength, λ_x, as a function of intrinsic period τ_i. Our present results are distributed in a range of periods from 2 to10 hrs, horizontal scales from 500 to 3000 km and vertical wavelengths from 10 to 80 km. As shown in the figure (by straight lines), all of the wave parameters fall within the range of linear gravity wave theory (Hines, 1960; Jones, 1969). The shaded area in the figure demonstrates Nakamura *et al.*'s (1993) results. Their results are grouped in the vertical wavelength region of 5 to 14 km, where our present technique (OH photometer) is difficult to identify.

The relationship between the horizontal and vertical wavelength is shown in Fig. 15. The two parameters are on logarithmic scale. It should be emphasized that these values are intrinsic, not inferred by using any assumptions. Although the number of points is rather small, it seems that the two parameters are positively correlated, i.e., the longer the horizontal wavelength the longer the vertical wavelength. From the linear gravity wave theory, horizontal and vertical wavelength are linearly related for a given wave period (Jones, 1969). The straight line in the figure indicates horizontal and vertical wavelength relation with a wave period of 4.0 h. The observed waves with the period between 3.5 and 4.5 hours listed in Table 6 are close to the straight line. Agreement between the experimental results and the linear gravity theory indicates that the airglow OH emission layer responds to gravity wave passage in a linear form (without any non-linear modulation), at least for the wave range presented here.

6. Concluding Remarks

Spatial variation of the airglow OH (6, 2) emission intensity and its rotational temperature and upper mesospheric wind system were measured simultaneously from Shigaraki (34.9°N, 136.1°E) in November 1994 and July 1995. The observations made it possible to detect atmospheric wave propagation and to determine intrinsic wave parameters in the upper mesosphere. Between the two different observation techniques, optical (airglow spectrophotometer) and radio frequency (MU radar), there is reasonable agreement on the inferred wave characteristics, i.e., horizontal and vertical wavelengths, period, phase velocity, and direction of propagation. Since the MU radar makes a direct measurement of the vertical wavelength, and the OH spectrophotometer makes a direct measurement of the horizontal wavelength, the two techniques are mutually complementary.

Through the two observation campaigns, November 1994 and July 1995, gravity waves with intrinsic periods of 2.1 to 9.2 hours, horizontal wavelengths of 480 to 2900 km, vertical wavelengths of 12 to 76 km, and phase speeds of 37 to 240 m/s were identified. On some occasions a short period (~3 h) gravity wave was observed to propagate, superposed on a long period (~9 h) wave, and/or two waves were observed to propagate in different directions. These wave parameters fall within the range of linear gravity wave theory. Agreement between the horizontal and vertical wavelengths obtained by optical and radar techniques shows the efficiency of the linear gravity wave theory for the presently observed wave range.

It should be emphasized that it is essential to measure background wind simultaneously when the gravity wave is to be studied by observing airglow images. The intrinsic phase velocity sometimes has the same order of magnitude as the background wind speed. On some occasions, it was also found that the variations of the rotational temperature and the intensity of the OH emission were 180° out of phase. The phase difference for different gravity wave character-

istics has been investigated from photochemical-dynamical modeling (e.g., Makhlouf *et al.*, 1995). Further observational investigation of the OH airglow response to gravity waves would be necessary.

Acknowledgments. The authors are grateful to Dr. B. R. Clemesha for useful discussions and help in revising the manuscript. The present experiment was carried out as a cooperative program between the Radio Atmospheric Science Center, RASC, Kyoto University and the Instituto Nacional de Pesquisas Espaciais, INPE/MCT. The authors are also grateful to Dr. M. Yamamoto and Dr. D. Yamanaka for their constant help and suggestions, and to Agnaldo Eras and Fabiola B. Costa for their technical support. The MU radar belongs to and is operated by the Radio Atmospheric Science Center, Kyoto University. This work was supported by the CNPq and JSPS under contract 910272/93.0.

References

Anderson, N., On the calculation of filter coefficients for maximum entropy spectral analysis, *Geophys.*, **39**, 69–72, 1974.

Bates, D. R. and M. Nicolet, The photochemistry of atmospheric water vapor, *J. Geophys. Res.*, **55**, 301, 1950.

Coxon, J. A. and S. C. Foster, Rotational analyses of hydroxyl vibration-rotation emission bands: molecular constants for OH X2Pi, $6 < v < 10$, *Can. J. Phys.*, **60**, 41, 1982.

Fukao, S., T. Sato, T. Tsuda, S. Kato, K. Wakasugi, and T. Makihira, The MU radar with an active phased array system, 1. Antenna and power amplifiers, *Radio Sci.*, **20**, 1155–1168, 1985a.

Fukao, S., T. Sato, T. Tsuda, S. Kato, K. Wakasugi, and T. Makihira, The MU radar with an active phased array system, 2. In-house equipment, *Radio Sci.*, **20**, 1169–1176, 1985b.

Gardner, C. S. and D. G. Voelz, Lidar studies of the nighttime sodium layer over Urbana, 2, Gravity waves, *J. Geophys. Res.*, **92**, 4673, 1987.

Hines, C. O., Internal atmospheric gravity waves at ionospheric heights, *Can. J. Phys.*, **38**, 1441, 1960.

Jones, W. L., Ray tracing for internal gravity waves, *J. Geophys. Res.*, **74**(8), 2028–2033, 1969.

Kato, S., Earth's atmosphere in dynamic coupling envisaged through atmospheric tides and atmospheric gravity waves: A view on the past-present-future research, *J. Geophys. Res.*, **101**(A5), 10577–10585, 1996.

Kaveh, M. and G. A. Lippert, An optimum tapered Burg method for linear prediction and spectral analysis, *IEEE Transactions Acoustics. Speech and Sig. Proceeding. ASSP*, **31**, 438–444, 1983.

Krassovsky, V. I. and M. V. Shagaev, Inhomogeneities and wavelike variations of the rotational temperature of atmospheric hydroxyl, *Planet. Space Sci.*, **22**, 1334–1337, 1974.

Krassovsky, V. I., B. P. Potapov, A. I. Semenov, M. V. Shagaev, N. N. Shefov, V. G. Sobolev, and T. I. Toroshelidze, Internal gravity waves near the mesopause and the hydroxyl emission, *Ann. Geophysique.*, **33**, 347–356, 1977.

Makhlouf, U. B., R. H. Picard, and J. R. Winick, Photochemical-dynamical modeling of the measured response of airglow to gravity waves, *J. Geophys. Res.*, **100**, 11289–11311, 1995.

Manson, A. H., Gravity wave horizontal and vertical wavelengths: An update of measurements in the mesopause region (∼80–100 km), *J. Atmos. Sci.*, **47**(23), 2765, 1990.

Manson, A. H. and C. E. Meek, Gravity wave propagation characteristics (60–120 km) as determined by the Saskatoon MF radar (Gravnet) system: 1983–1985 at 52°N, *J. Atmos. Sci.*, **45**, 932–946, 1988.

Mies, F. H., Calculated Vibrational Transition Probabilities of OH (X2II), *J. Molecular Spectroscopy.*, **53**, 150–188, 1974.

Moreels, G. and M. Herse, Photographic evidence of waves around the 85 km level, *Planet. Space Sci.*, **25**, 265–273, 1977.

Nakamura, T., T. Tsuda, M. Tsutsumi, K. Kita, T. Uehara, S. Kato, and S. Fukao, Meteor wind observations with the MU radar, *Radio Sci.*, **26**, 857–869, 1991.

Nakamura, T., T. Tsuda, M. Yamamoto, S. Fukao, and S. Kato, Characteristics of gravity waves in the mesosphere observed with the MU radar, 2. Propagation direction, *J. Geophys. Res.*, **98**, 8911–8923, 1993.

Pendleton, W. R. J., P. J. Espy, and M. R. Hammond, Evidence for non-local-thermodynamic-equilibrium rotation in the OH nightglow, *J. Geophys. Res.*, **98**, 11567, 1993.

Peterson, A. W., Airglow events visible to the naked eye, *Appl. Optics*, **18**, 3390–3393, 1979.

Shefov, N. N. and T. I. Toroshelidze, Dynamics of minor constituent emissions, *Ann. Geophysique.*, **30**, 79, 1974.

Swenson, G. R. and C. S Gardner, Preface for "The 1993 airbone Lidar and Observations of the Hawaiian Airglow/Airbone Noctilucent cloud campaigns", *J. Geophys. Res.*, **103**(D6), 6249–6250, 1998.

Takahashi, H., B. R. Clemesha, Y. Sahai, P. P. Batista, and D. M. Simonich, Seasonal variations of mesospheric hydrogen and ozone concentrations derived from ground-nased airglow and lidar observations, *J. Geophys. Res.*, **97**, 5987, 1992.

Takahashi, H., P. P. Batista, R. A. Buriti, D. Gobbi, T. Nakamura, T. Tsuda, and S. Fukao, Simultaneous measurements of airglow OH emission and meteor wind by a scanning photometer and the MU radar, *J. Atmos. Sol.-Terr. Phys.*, **60**, 1649–1668, 1998.

Taylor, M. J., P. J. Espy, D. J. Baker, R. J. Sica, P. C. Neal, and W. R. Pendleton, Jr., Simultaneous intensity, temperature and imaging measurements of short period wave structure in the OH nightglow emission, *Planet. Space Sci.*, **39**, 1171–1188, 1991.

Taylor, M. J., D. C. Fritts, and J. R. Isler, Determination of horizontal and vertical structure of a novel pattern of short period gravity waves imaged during ALOHA-93, *Geophys. Res. Lett.*, **22**(20), 2837–2840, 1995a.

Taylor, M. J., M. B. Bishop, and V. Taylor, All-sky measurements of short waves imaged in the OI (557.7 nm), Na (589.2 nm) and near infrared OH and O_2 (0, 1) nightglow emissions during the ALOHA-93 campaign, *Geophys. Res. Lett.*, **22**(20), 2833–2836, 1995b.

Taylor, M. J., W. R. Pendleton, Jr., S. Clark, H. Takahashi, G. Gobbi, and R. A. Goldberg, Image measurements of short-period gravity waves at equatorial latitudes, *J. Geophs. Res.*, **102**(D22), 26283–26299, 1997.

Tsuda, T., S. Kato, A. H. Manson, and C. E. Meek, Characteristics of semidiurnal tides observed by the Kyoto meteor radar and Saskatoon medium-frequencdy radar, *J. Geophys. Res.*, **93**(D6), 7027–7036, 1988.

Tsuda, T., T. Inoue, D. C. Fritts, T. E. VanZandt, S. Kato, T. Sato, and S. Fukao, MST radar observations of a saturated gravity wave spectrum, *J. Atmos. Sci.*, **46**, 2440–2447, 1989.

Tsuda, T., S. Kato, T. Yokoi, T. Inoue, M. Yamamoto, T. E. Vanzandt, S. Fukao, and T. Sate, Gravity waves in the mesosphere observed with the middle and upper atmosphere radar, *Radio Sci.*, **26**, 1005–1018, 1990.

Tsutsumi, M., T. Tsuda, T. Nakamura, and S. Fukao, Temperature fluctuations near the mesopause inferred from meteor observations with the middle and upper atmosphere radar, *Radio Sci.*, **29**, 599–610, 1994.

Turnbull, D. N. and R. P. Lowe, New hydroxyl transition probabilities and their importance in airglow studies, *Planet. Space Sci.*, **37**, 723–738, 1989.

Walterscheid, R. L. and G. Schubert, Dynamical-chemical model of fluctuations in the OH airglow driven by migrating tides, stationary tides, and planetary waves, *J. Geophys. Res.*, **100**, 17443–17449, 1995.

Walterscheid, R. L., G. Schubert, and M. P. Hickey, Comparison of theories for gravity wave induced fluctuations in airglow emissions, *J. Geophys. Res.*, **99**, 3935, 1994.

Zhang, S. P., R. N. Peterson, R. H. Wiens, and G. G. Shepherd, Gravity Waves from O_2 nightglow during the AINDA '89 campaign I: emission rate/temperature observations, *J. Atmos. Terr. Phys.*, **55**, 355, 1993.

H. Takahashi (e-mail: hisao@laser.inpe.br), P. P. Batista, R. A. Buriti, D. Gobbi, T. Nakamura, T. Tsuda, and S. Fukao